applied sciences

MDPI

Article

Intelligent Safety Assessment of Island Longwall Roadway Integrating Asymmetric Physical Features and Cost-Sensitive Learning

Weichen Fang [1,2], Yang Song [1,3,*], Dexing He [1,3], Jinsong He [1,3], Ningning Chen [1,3], Haotian Feng [1,3], Junyue Fan [1,3] and Xinqiu Fang [1,3]

[1] School of Mines, China University of Mining and Technology, Xuzhou 221116, China; weichen.fang@student.uq.edu.au (W.F.); tb23020045p41@cumt.edu.cn (D.H.); ts23020120p31@cumt.edu.cn (J.H.); ningningchen@cumt.edu.cn (N.C.); fenghaotian@cumt.edu.cn (H.F.); tb25020016a41@cumt.edu.cn (J.F.); xinqiufang@cumt.edu.cn (X.F.)
[2] School of the Environment, Faculty of Science, The University of Queensland, St Lucia, Brisbane, QLD 4072, Australia
[3] Research Center of Intelligent Mining, China University of Mining and Technology, Xuzhou 221116, China
* Correspondence: song.yang@cumt.edu.cn; Tel.: +86-198-5208-0929

Abstract

Roadways serving island longwall panels are highly susceptible to severe asymmetric deformation under extreme eccentric loading from multiple adjacent goafs. To address the difficulties in characterizing the surrounding rock load imbalance and the high false-negative rates of conventional algorithms under extremely imbalanced monitoring data, an intelligent assessment method integrating spatially asymmetric physical features with cost-sensitive learning was developed. Implicit equation analysis and numerical simulation clarified the mechanical mechanism by which principal stress axis deflection induces butterfly-shaped asymmetric rotational failure, enabling the construction of dimensionless integrated asymmetry and structural transfer asymmetry coefficients. Reconstruction of the cost-sensitive objective function increased the recall rate for hazardous samples from 37.5% (baseline model) to 92.2%, while maintaining a precision of 96.7%. Following the field implementation of a three-tier differentiated roadway control scheme, the integrated asymmetry coefficients at critically eccentrically loaded stations (i.e., Station 12 and Station 07) remained below 0.2 during the monitoring period, enabling real-time intelligent perception and proactive stability control of roadways subjected to complex eccentric loading. Ultimately, this study confirms the viability of integrating physics-informed features with machine learning, demonstrating significant potential for advancing the transition toward intelligent and proactive safety management in complex underground construction.

Keywords: island longwall panel; asymmetric deformation; cost-sensitive learning; safety assessment; differentiated control

Check for updates

Academic Editor: Nikolaos Koukouzas

Received: 30 July 2026
Revised: 28 August 2026
Accepted: 31 August 2026
Published: 2 September 2026

Copyright: © 2026 by the authors. Licensee MDPI, Basel, Switzerland. This article is an open access article distributed under the terms and conditions of the Creative Commons Attribution (CC BY) license.

1. Introduction

Island longwall panels created by skip mining are widely employed to maximize coal resource recovery. However, because such panels are bounded by goafs on two or more sides, their surrounding rock is commonly subjected to intense superposition of static and dynamic loads and to eccentric loading. These conditions readily induce severe asymmetric roadway deformation, wall extrusion, and floor heave, thereby threatening mine safety [1,2]. Accurate, forward-looking, and highly sensitive assessment of roadways

under eccentric loading, coupled with targeted differentiated control of the surrounding rock, is therefore a critical challenge in controlling the stability of deep underground spaces.

The loading, deformation, and instability of underground roadways and coal pillars under mining disturbance have been studied extensively. For the mechanical evolution of the surrounding rock, Carranza-Torres [3] and Vlachopoulos [4] established the convergence–confinement framework for coupled surrounding rock support analysis, whereas Diederichs [5] examined in situ yielding models and damage threshold boundaries for highly stressed rock masses. Building on this foundation, Yujie Ma et al. [6], Qiang Fu et al. [7], and Peng Huang et al. [8] analyzed the loading characteristics of coal pillars and roadways in island panels or settings affected by multiple goafs. They elucidated how the superposition of the lateral abutment pressure from adjacent goafs and the front abutment pressure from the active panel deflects the surrounding rock stress axes, generates large stress contrasts between the two roadway walls, and drives severe asymmetric expansion of the plastic zone. Shihang Li et al. [9], Zhijie Zhu et al. [10], and Qiang Zhang et al. [11] further demonstrated how single- and double-peaked vertical stress evolution, the principal stress ratio, and the size of the central elastic core govern the ultimate bearing capacity and overall stability of panel pillars. To mitigate severe eccentric loading failure in nonuniform stress fields, Tao Ding et al. [12], Wanpeng Huang et al. [13], and Sakhno et al. [14] proposed coordinated control strategies that interrupt vertical stress transfer through roof hydraulic fracturing or slotting-induced pressure relief and reinforce the load-bearing structure using rigid concrete walls, grouting, or anti-shear piles. These studies provide a physical and mechanical framework for understanding imbalanced instability under complex mining disturbance; however, real-time, zone-specific precision support based on surrounding rock deformation remains insufficiently explored.

Concurrently, advances in the Internet of Things and data science have promoted intelligent roadway stability assessment and hazard warning based on multi-source monitoring data. For multi-source sensing and feature extraction, Kajzar et al. [15], Singh et al. [16], and Lee [17] continuously captured nonuniform deformation of roadway cross-sections using three-dimensional laser scanning and photogrammetry. Hudecek et al. [18] developed a dynamic method for evaluating coal pillar loading, whereas Satici et al. [19] combined monitored deformation with numerical simulation to back-analyze excavation-damaged-zone thickness. To identify physical precursors of deep surrounding-rock failure, Yuanguang Zhu et al. [20], Kai Zhan et al. [21], and Wenwei Wang et al. [22] used acoustic emission, microseismic monitoring, measurement-while-drilling features, and elastic energy storage release patterns to characterize progressive failure and energy release during the transition from microscopic tensile spalling to macroscopic shear instability. For intelligent classification and prediction of safety states, Xinqiu Fang et al. [23], Bemah Ibrahim et al. [24], Gengxin Li et al. [25], Tao Ma et al. [26], and Feng Cui et al. [27] introduced ensemble or deep learning algorithms together with game theoretic interpretability methods and spatially gridded datasets. Their models classified and predicted excavation damaged zone thickness, rock bolt failure risk, and microseismic damage level, enabling early warning. Dongmei Huang et al. [28] and Shenggang Wang et al. [29] additionally applied combined weighting and multilevel matter element extension theory to quantify the coupled effects of multiple factors on surrounding rock collapse risk. Furthermore, advanced machine learning architectures, such as multi-output chained models that integrate target variables into the input dataset, have recently demonstrated significant superiority in simultaneously predicting multiple evaluation indicators with extremely high accuracy [30]. Despite this progress, major limitations remain: purely data-driven algorithms act as uninterpretable black boxes lacking mechanical priors, the difficulty of extracting spatially asymmetric physical features that represent load imbalance in the surrounding rock, and the high rate

of missed hazardous events produced by conventional intelligent algorithms when applied to extremely imbalanced time-series monitoring data.

Here, the intelligent safety assessment and differentiated control of the 2206 return airway at the Xiaohuigou Coal Mine, a representative island panel roadway, were investigated by integrating asymmetric physical features with cost-sensitive learning. Initially, the deflection of principal stress axes and the resulting butterfly-shaped rotational shear failure in the floor driven by nonuniform boundary stiffness were elucidated. Subsequently, dimensionless surrogate physical features, including integrated asymmetry and structural transfer asymmetry indices, were constructed based on the nonuniform load redistribution and transfer within the surrounding rock. On this basis, the XGBoost loss function was reconstructed using nonlinear penalty weights and integrated with forward rolling time-series cross-validation, establishing a four-level intelligent roadway safety assessment model and delineating axial risk levels. Finally, a three-tier differentiated control scheme was proposed and validated along the roadway axis. By translating mechanical understanding into the machine learning feature space, this study provides a systematic framework for the safety assessment and precision control of island panel roadways subjected to complex eccentric loading.

2. Case Study

2.1. Engineering Background

The Xiaohuigou Coal Mine is located in Qingxu County, Taiyuan, Shanxi Province, China. The 2206 working face lies between the 2202 and 2204 goafs and therefore constitutes a typical island longwall panel (Figure 1a). The No. 2 coal seam in the second mining district, 5.1 m vertically below the overlying No. 3 coal seam, was being extracted. The seam has an average thickness of 2.77 m and an average dip of 3°. The working face was 210 m wide and had a total advance length of 1580 m.

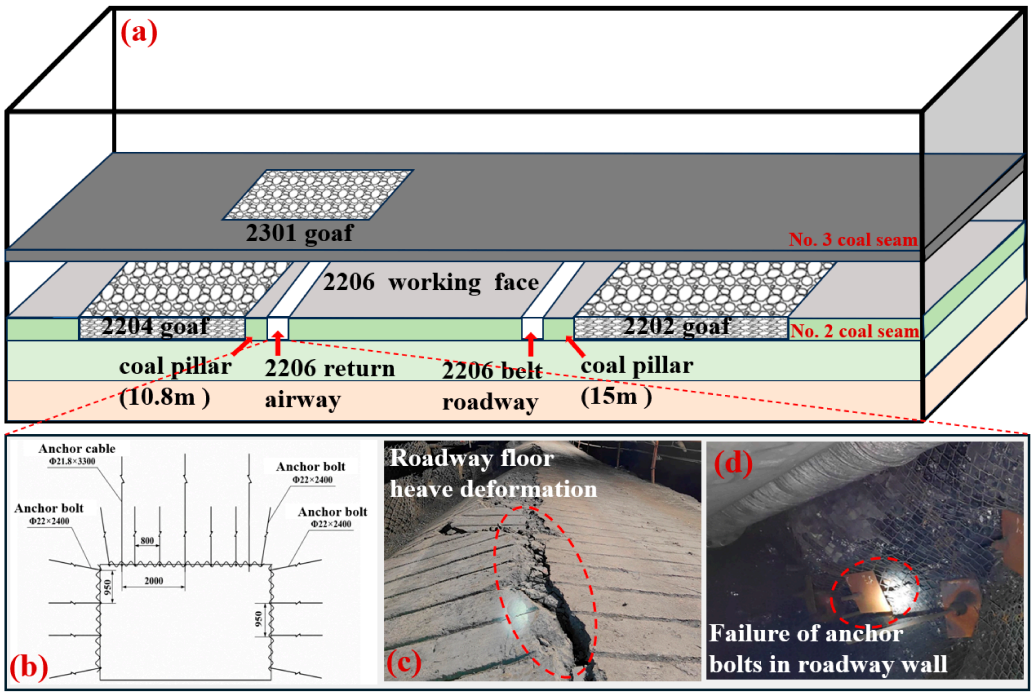

Figure 1. Layout and field conditions of 2206 island longwall panel. (**a**) Spatial layout of the working face; (**b**) Support design of the roadway; (**c**) Roadway floor heave deformation; (**d**) Failure of anchor bolts in the roadway wall.

A 10.8 m narrow coal pillar separated the 2206 return airway from the 2204 goaf, and the 580–672 m section of the airway was overlain by the 2301 goaf. The roadway had a rectangular cross-section measuring 5.2 m × 3.5 m and was supported by anchor bolts, anchor cables, beams, and mesh (Figure 1b). Field observations during roadway excavation recorded frequent coal-bump sounds and pronounced floor heave at multiple locations (Figure 1c). The shallow surrounding rock on both walls was heavily fractured, and parts of the shallow support had failed (Figure 1d). Coal was extruded from the shoulder of the coal pillar side, anchor bolt and cable plates curled at their edges, and several anchor bolts fractured.

2.2. Physical and Mechanical Properties of Coal and Rock

Uniaxial compressive strength, Brazilian tensile strength, and shear strength tests were conducted on coal and rock specimens to determine the physical and mechanical parameters of the surrounding rock of the 2206 island panel roadway (Figure 2). The results (Table 1) showed that the No. 2 coal seam had a uniaxial compressive strength of only 5.96 MPa, a tensile strength of 0.30 MPa, a cohesion of 1.33 MPa, and an internal friction angle of 28°, indicating limited self-supporting capacity and low resistance to deformation and failure. By contrast, the uniaxial compressive strengths of the immediate roof (sandy mudstone) and immediate floor (sandstone) were 46.69 and 56.02 MPa, respectively. These measurements provided the parameter basis for surrounding rock stability analysis and support design.



(**a**) Uniaxial compression test (**b**) Brazilian tensile test (**c**) Shear test

Figure 2. Mechanical tests characterizing representative coal and rock specimens.

Table 1. Physical and mechanical properties of rock surrounding test roadway.

Sampling Location	Lithology	Density/(kg·m^{-3})	Uniaxial Compressive Strength/(MPa)	Tensile Strength/(MPa)	Cohesion/(MPa)	Internal Friction Angle/(°)
Immediate roof	Sandy mudstone	2650	46.69	6.15	9.29	34
No. 2 coal	Coal	1500	5.96	0.30	1.33	28
Immediate floor	Sandstone	2650	56.02	5.88	11.83	35

3. Asymmetric Roadway Failure Under Eccentric Loading: Characteristics and Mechanical Analysis

3.1. Mechanical Analysis of Asymmetric Surrounding Rock Failure Under Eccentric Loading

The asymmetric failure of an island panel roadway originates from nonuniform static and dynamic eccentric loading induced by overburden movement. The 2206 return airway was analyzed as a representative case. A narrow coal pillar was on its left side and a semi-infinite solid coal mass on its right, producing a pronounced contrast in vertical stiffness across the roadway. This contrast caused differential subsidence of the overlying T-shaped bidirectional cantilever-hinged structure (Figure 3).

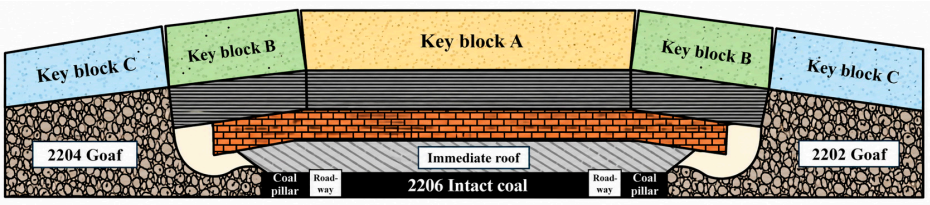

Figure 3. Key blocks from overburden structure above island longwall panel.

According to limit equilibrium theory [31], the narrow coal pillar is subjected to lateral abutment pressure from both the goaf and the roadway. The limiting development depth x_0 of its plastic zone is expressed as:

$$x_0 = \frac{M}{2\lambda \tan \phi_0} \ln\left(\frac{K\gamma H + C\cot\phi}{\lambda(P_x + C\cot\phi)}\right) \tag{1}$$

Substitution of the measured parameters yielded plastic zone widths of 2.17 m and 2.06 m on the two sides of the narrow coal pillar, leaving an elastic core only 6.57 m wide. When the front dynamic load generated by extraction of the active panel was superimposed, the elastic core was readily crushed and entered a yielding state. The resulting differential overburden subsidence generated a rotational moment that deflected the vertical principal stress axis above the roadway by angle α, producing a far-field eccentrically loaded stress field with a high principal stress ratio $K = P_1/P_3$ (Figure 4a,b).

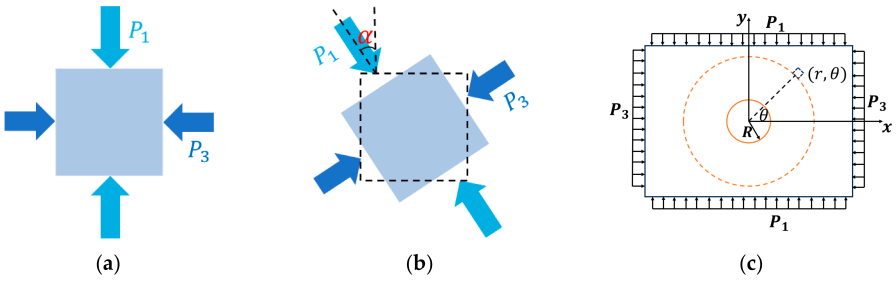

Figure 4. Principal stress distribution, deflection, and roadway coordinates define loading model. (**a**) Principal stress distribution; (**b**) Principal stress deflection; (**c**) Roadway Cartesian coordinate system.

Projecting the inclined principal stress field onto the roadway Cartesian coordinate system (Figure 4c) gives the boundary stress components:

$$\begin{cases} \sigma_x = \frac{P_1+P_3}{2} + \frac{P_1-P_3}{2}\cos 2\alpha \\ \sigma_y = \frac{P_1+P_3}{2} - \frac{P_1-P_3}{2}\cos 2\alpha \\ \tau_{xy} = \frac{P_1-P_3}{2}\sin 2\alpha \end{cases} \tag{2}$$

Here, the shear stress term $\tau_{xy} \neq 0$ mechanically drives the oblique rotation of the surrounding rock plastic zone.

Under the boundary conditions defined by Equation (2), the complex variable method and the classical Kirsch stress solution [32] yield the following general analytical solution for the stress field at any point (r, θ) in the surrounding rock:

$$\begin{cases} \sigma_r = \frac{\sigma_x+\sigma_y}{2}\left(1-\frac{a^2}{r^2}\right) + \frac{\sigma_x-\sigma_y}{2}\left(1-4\frac{a^2}{r^2}+3\frac{a^4}{r^4}\right)\cos 2\theta + \tau_{xy}\left(1-4\frac{a^2}{r^2}+3\frac{a^4}{r^4}\right)\sin 2\theta \\ \sigma_\theta = \left(1+\frac{a^2}{r^2}\right) - \frac{\sigma_x-\sigma_y}{2}\left(1+3\frac{a^4}{r^4}\right)\cos 2\theta - \tau_{xy}\left(1+3\frac{a^4}{r^4}\right)\sin 2\theta \\ \tau_{r\theta} = -\frac{\sigma_x-\sigma_y}{2}\left(1+2\frac{a^2}{r^2}-3\frac{a^4}{r^4}\right)\sin 2\theta + \tau_{xy}\left(1+2\frac{a^2}{r^2}-3\frac{a^4}{r^4}\right)\cos 2\theta \end{cases} \tag{3}$$

where R is the roadway radius.

Combining the Mohr–Coulomb strength criterion with the principal stress extrema yields the following eighth-order implicit equation for the plastic zone boundary R_p under the combined effects of principal stress deflection angle α and stress ratio K:

$$K_1\left(\frac{R_p}{R}\right)^8 + K_2\left(\frac{R_p}{R}\right)^6 + K_3\left(\frac{R_p}{R}\right)^4 + K_4\left(\frac{R_p}{R}\right)^2 + K_5 = 0 \tag{4}$$

where the mechanical coefficients K_1–K_5 depend on deflection angle α, stress ratio K, and friction angle φ:

$$\begin{cases} K_1 = 9(1-K)^2 \\ K_2 = -12(1-K)^2 + 6\left(1-K^2\right)\cos 2(\theta-\alpha) \\ K_3 = 2(1-K)^2\left[\left(5+2\sin^2\varphi\right)\cos^2 2(\theta-\alpha) - \sin^2 2(\theta-\alpha)\right] \\ K_4 = -4(1-K)^2\cos 4(\theta-\alpha) - 2\left(1-K^2\right)\left(1+2\sin^2\varphi\right)\cos 2(\theta-\alpha) \\ \quad - \frac{4C(1-K)\sin 2\varphi\cos 2(\theta-\alpha)}{P_3} \\ K_5 = (1-K)^2 - \sin^2\varphi\left(1+K+\frac{2C\cos\varphi}{P_1\sin\varphi}\right)^2 \end{cases} \tag{5}$$

Solving this eighth-order implicit equation gives the plastic zone boundary curves shown in Figure 5. The analytical solution indicated that a high principal stress ratio K controls the radial depth of nonuniform plastic zone expansion, whereas the principal stress axis deflection angle α controls the orientation of the asymmetric expansion.

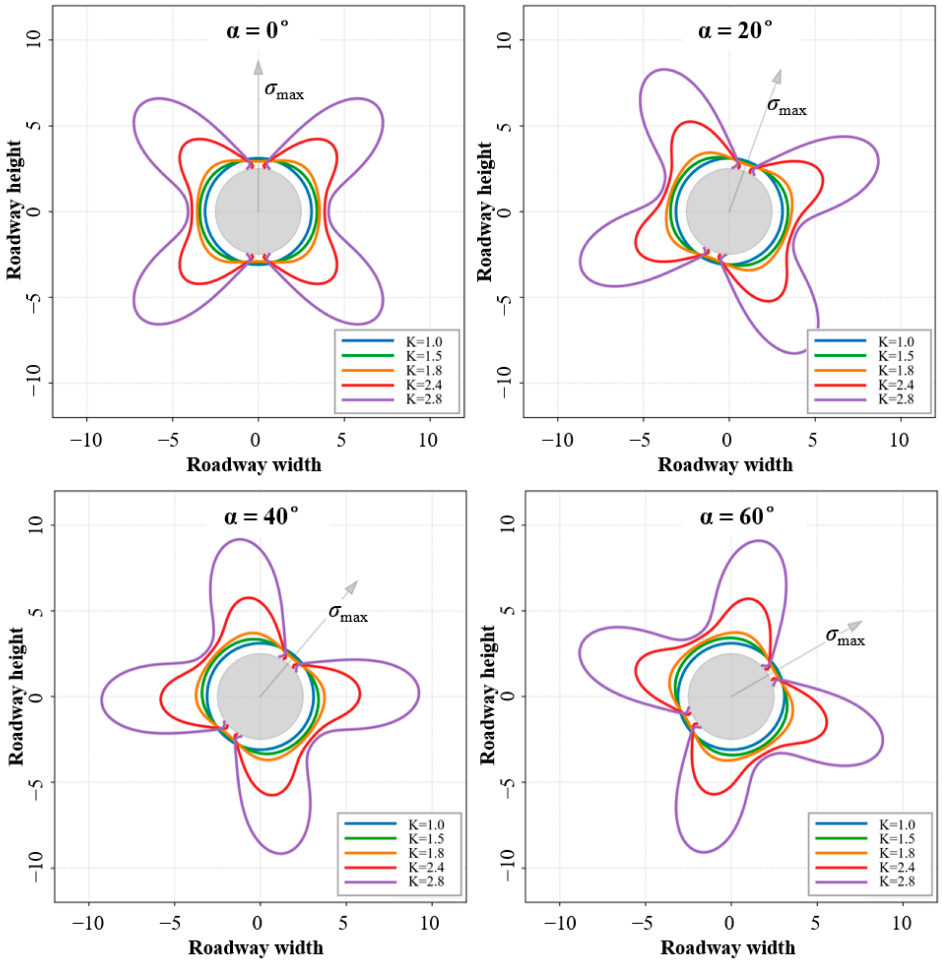

Figure 5. Analytical solution predicts butterfly-shaped asymmetric plastic zone development.

3.2. Numerical Simulation of Asymmetric Roadway Failure Evolution

A three-dimensional FLAC3D model was established to verify the evolution mechanism of asymmetric roadway failure (Figure 6). The model measured 840 m × 1400 m × 100 m and employed the Mohr–Coulomb constitutive model. A vertical load of 8.75 MPa was applied to the model top to represent the overburden weight, and the horizontal lateral pressure coefficient was set to 1.1. The simulation followed the actual extraction sequence: the overlying 2301 working face and the adjacent 2202 and 2204 working faces were extracted successively before the 2206 return airway was excavated. The principal physical and mechanical properties of the coal and rock are listed in Table 2. The roadway and narrow coal pillar regions were locally refined to balance computational accuracy and efficiency, whereas a coarser mesh was used near the outer boundaries, away from mining activity.

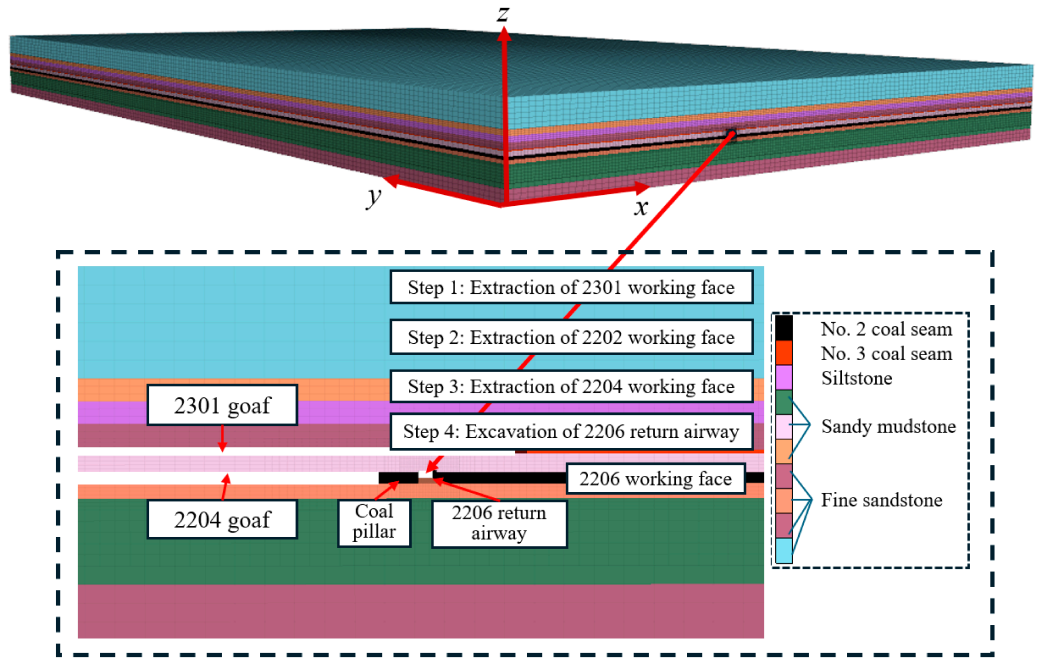

Figure 6. FLAC3D model reproduces sequential extraction around 2206 island longwall panel.

Table 2. Mechanical parameters assigned to model strata.

Stratum/Lithology	Density/(kg/m^3)	Bulk Modulus/(GPa)	Shear Modulus/(GPa)	Internal Friction Angle/(°)	Cohesion/(MPa)	Tensile Strength/(MPa)
Sandy mudstone	2660	7.64	3.73	34	5.5	4.9
Fine sandstone	2760	9.84	4.03	31	6.2	4.2
No. 2 coal	1500	0.91	0.42	28	1.33	0.3
No. 3 coal	1500	0.91	0.42	28	1.33	0.3
Mudstone	2500	4.86	3.15	30	3.2	2.3
Siltstone	2740	7.42	2.85	32	4.6	3.6

A continuous monitoring line was placed along the roadway axis at the upper-right shoulder of the 2206 return airway to extract the far-field dynamic stress field after complete superposition of disturbances from the surrounding goafs. The simulation results (Figure 7) showed pronounced axial zonation in principal stress ratio K and deflection angle α. Within the strongly superimposed disturbance zone near the stop-mining lines of the 2204 and 2301 goafs (chainage 530–700 m), K rose abruptly to an eccentric loading peak of 2.4, while α fluctuated sharply within the high range of 40–60°.

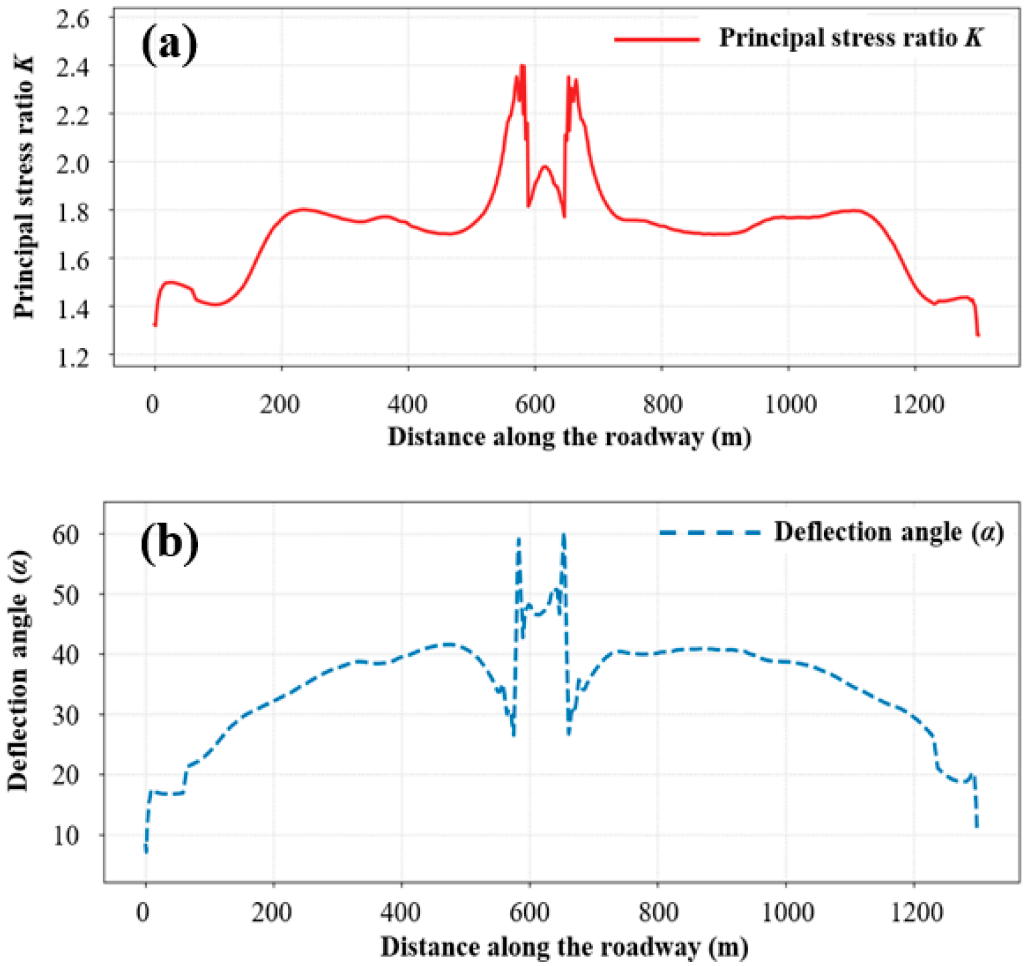

Figure 7. Principal stress ratio and principal stress axis deflection vary along return airway: (**a**) principal stress ratio K; (**b**) deflection angle α.

Plastic zone slices of the roadway cross-section (Figure 8) were examined to verify this evolution. In the solid coal section (0–150 m), the plastic zone developed regularly and symmetrically and remained concentrated in the two walls. Beyond the stop-mining line, principal stress deflection induced by lateral abutment pressure from the 2204 goaf caused the plastic zone to extend obliquely and asymmetrically; its development reached a maximum near the 2301 and 2202 stop-mining lines. At 10 m from the 2301 stop-mining line, the failure depths on the coal pillar and solid coal sides were 5 m and 4 m, respectively. Load transfer from 2301 goaf increased the roof failure depth to 5.5 m; failure extended 2.5 m into the central floor, and severe shear slip occurred on the coal pillar side. Directly beneath the pressure-relief protection zone of the 2301 goaf, load transfer from caved strata placed the surrounding rock in a low-stress field and produced relatively uniform plastic development. Nevertheless, historical mining had already plastically damaged rock within 4 m above the roof. After the roadway passed beyond the 2301 goaf and entered the zone affected by goafs on both sides, loss of pressure-relief protection produced diagonally opposed, through-going plastic zones. Finally, after the roadway crossed the 2204 goaf boundary and entered solid coal, the eccentric loading effect vanished and the plastic zone contracted to a symmetric elliptical form.

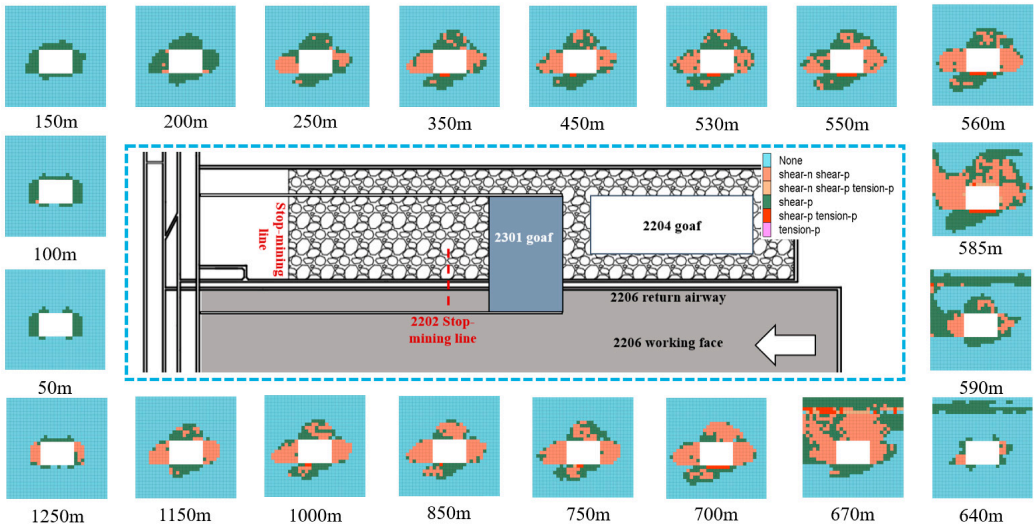

Figure 8. Plastic-zone geometry evolves markedly along the return airway.

4. Intelligent Roadway Safety Assessment Using Improved XGBoost Model

4.1. Monitoring Data and Construction of Asymmetry Features

To monitor the mechanical response and stability of the surrounding rock in the 2206 return airway during extraction, anchor bolt and cable load cells, roof extensometers, and borehole stress meters were installed to form a multi-source real-time monitoring network (Figure 9). Five comprehensive monitoring stations and 19 general monitoring stations were arranged in 300 m intervals along the roadway axis. The network continuously recorded deep and shallow roof separation, anchor bolt and cable loads, and borehole stresses at different depths in both roadway walls, thereby providing real-time measurements of ground pressure response.

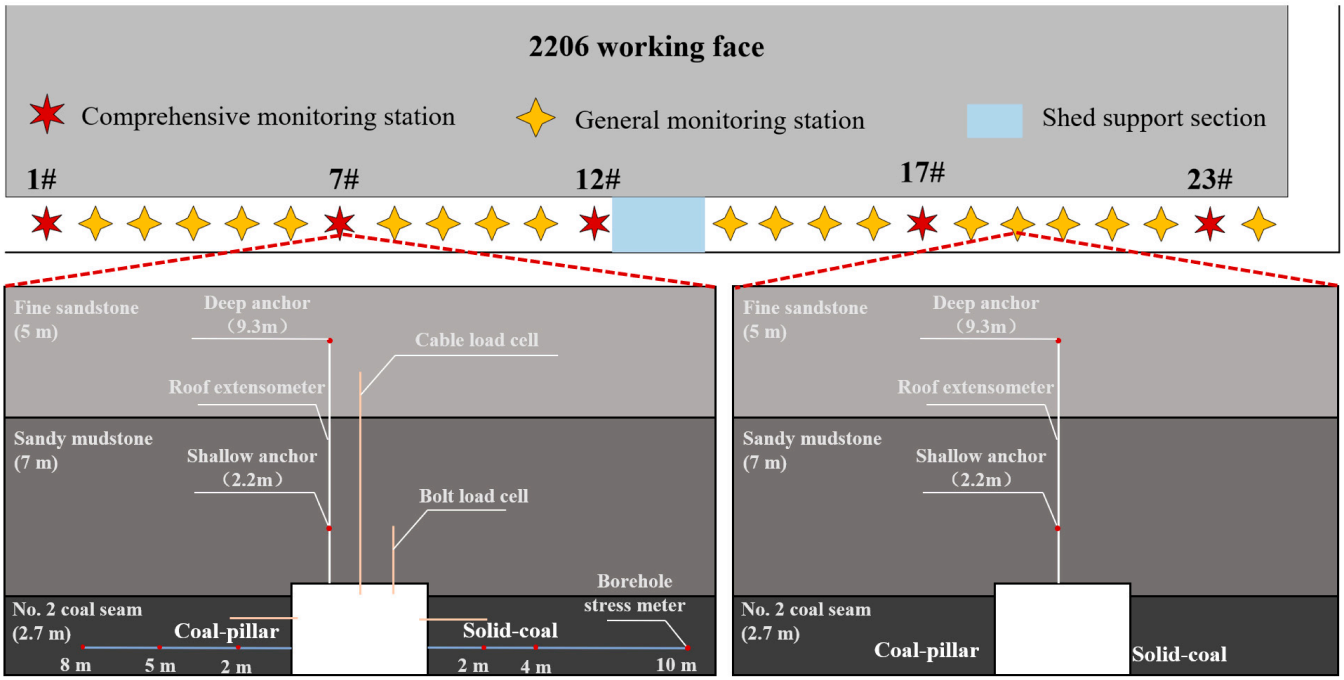

Figure 9. Multi-source network monitors roadway surrounding rock in real time.

Compared to purely data-driven features, constructing physical features offers three critical advantages. First, it ensures engineering interpretability, directly identifying the orientation of load imbalances to guide support design. Second, it embeds mechanical prior knowledge, forcing the algorithm to focus on spatial gradients rather than raw stress fluctuations. Third, it acts as domain knowledge regularization, enhancing robustness against random sensor noise. Therefore, because micromechanical parameters such as deep principal stress axis deflection angle α and principal stress ratio K cannot be measured directly underground, four dimensionless indices were constructed from nonuniform load redistribution and load transfer to represent spatial loading imbalance in the surrounding rock support system:

(1) Stress spatial asymmetry coefficient (K_{Stress}) quantifies the difference in deep surrounding rock stress between the left and right roadway walls:

$$K_{\text{Stress}} = \frac{\left|\sigma_{\text{rock}}^{L} - \sigma_{\text{rock}}^{R}\right|}{\sigma_{\text{rock}}^{L} + \sigma_{\text{rock}}^{R} + \varepsilon} \tag{6}$$

(2) Support spatial asymmetry coefficient (K_{Bolt}) characterizes nonuniform loading of the anchor bolt support structures on the two roadway walls:

$$K_{\text{Bolt}} = \frac{\left|\sigma_{\text{bolt}}^{L} - \sigma_{\text{bolt}}^{R}\right|}{\sigma_{\text{bolt}}^{L} + \sigma_{\text{bolt}}^{R} + \varepsilon} \tag{7}$$

(3) Integrated asymmetry coefficient (K_{AFC}) combines surrounding rock stress and support response at a 3:2 weighting ratio to represent the overall asymmetric loading state of the roadway cross-section:

$$K_{\text{AFC}} = 0.6 \times K_{\text{Stress}} + 0.4 \times K_{\text{Bolt}} \tag{8}$$

(4) Structural transfer asymmetry coefficient (K_{STA}) uses the one-sided stress-transfer ratios η_L and η_R to quantify spatial heterogeneity in the rate at which surrounding rock pressure is transferred to the shallow support structure:

$$\eta_L = \frac{\sigma_{\text{bolt}}^{L}}{\sigma_{\text{rock}}^{L} + \varepsilon},\ \eta_R = \frac{\sigma_{\text{bolt}}^{R}}{\sigma_{\text{rock}}^{R} + \varepsilon} \tag{9}$$

$$K_{\text{STA}} = \frac{|\eta_L - \eta_R|}{\eta_L + \eta_R + \varepsilon} \tag{10}$$

Here, σ_{rock} and σ_{bolt} are the measured deep borehole stress and anchor bolt tensile–compressive load, respectively; superscripts L and R denote the left wall (coal pillar side) and right wall (solid coal side), respectively; and ε is a numerical stability constant (10^{-6}).

4.2. Predictive Model Development and Performance Evaluation

Currently, rational supervised learning algorithms, such as support vector machines, random forests, and standard gradient boosting, are widely employed for safety status classification. However, to effectively capture rare hazardous events under the extreme class imbalance (2324:1) present in our monitoring data, the cost-sensitive XGBoost with dynamic penalty weights was definitively chosen as the primary approach. In addition, when evaluating the instability of underground spaces, especially those near goaf areas [33], the method of using reduced dimensional space to replace features is highly representative and efficient compared to using computationally intensive 3D regression models.

Monitoring data collected from the 2206 return airway between 20 March and 17 November 2025 were compiled. Engineering codes, observed instability patterns, theoretical calculations, and safety factor reduction were then used to establish four safety-state labels: Level I (stable), Level II (attention), Level III (warning), and Level IV (danger).

As shown in Table 3, the dataset was highly imbalanced: Level I (stable) samples accounted for 95.71%, whereas Level IV (danger) samples, the primary detection target, accounted for only 0.04%, giving a maximum interclass imbalance ratio of 2324:1. To prevent majority-class dominance from causing high false-negative risk in conventional classifiers, a nonlinear cost-sensitive weight w_i was introduced to modify the XGBoost loss function. At iteration t, the objective function was reconstructed as:

$$L^{(t)} = \sum_{i=1}^{n} w_i l\left(y_i, \hat{y}_i^{(t-1)} + f_t(x_i)\right) + \Omega(f_t) \tag{11}$$

Table 3. Distribution of roadway surrounding rock safety-state samples.

Label Class	Number of Samples	Proportion (%)
Level I (stable)	264948	95.71%
Level II (attention)	6313	2.28%
Level III (warning)	5435	1.96%
Level IV (danger)	114	0.04%

The reconstructed objective function was expanded to second order using a Taylor series, and the leaf nodes were regrouped to obtain the optimal output weight of leaf node j, w_j^*, and the corresponding tree-structure score L^*:

$$w_j^* = -\frac{\widetilde{G}_j}{\widetilde{H}_j + \lambda} \tag{12}$$

$$L^* = -\frac{1}{2}\sum_{j=1}^{T} \frac{\widetilde{G}_j^2}{\widetilde{H}_j + \lambda} + \gamma T \tag{13}$$

Here, $\widetilde{G}_j = \sum_{i \in I_j} w_i g_i$ and $\widetilde{H}_j = \sum_{i \in I_j} w_i h_i$ denote the accumulated first- and second-order derivatives, respectively; λ and γ are regularization penalty coefficients.

Because the ground pressure monitoring data exhibited strong temporal dependence, forward rolling window time-series cross-validation was applied to prevent information leakage. Subject to the engineering constraint that fewer than 5% of Level III (warning) samples could be incorrectly escalated to Level IV (danger), grid search identified an optimal penalty weight ratio of 1:2:10:60 for the four classes (stable: attention: warning: danger).

The performance results (Table 4) showed that the conventional model recalled only 37.5% of danger samples, indicating a substantial false-negative safety risk. After cost-sensitive modification, recall for danger samples increased to 92.2%, while precision remained at 96.7%. The cross-model comparison (Figure 10) further showed that the improved model achieved a better balance between low false-negative and false-positive rates than random forest, a backpropagation neural network, and LightGBM.

Table 4. Performance of improved and baseline models.

Model	Macro Precision	Macro Recall	Macro F1	Macro F2	Danger Class Precision	Danger Class Recall	Danger Class F1-Score
Baseline model	0.729	0.778	0.744	0.761	0.421	0.375	0.397
Improved model	0.822	0.861	0.827	0.842	0.967	0.922	0.944

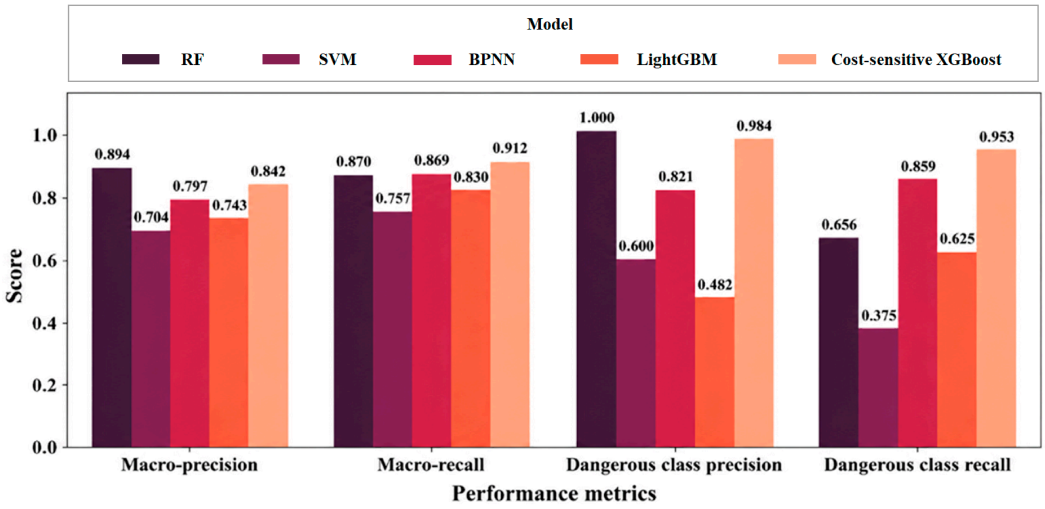

Figure 10. Cost-sensitive XGBoost model outperformed comparison models.

Furthermore, a robustness validation was conducted for different unbalance ratios. By preserving the minority class (Levels III and IV) and stratifying downsampling the majority class (Levels I and II), synthetic datasets with varying imbalance ratios (1000:1, 500:1, and 100:1) were generated. The proposed forward rolling-window grid search framework was reapplied to these subsets. As demonstrated in Table 5, the framework adaptively identified milder optimal penalty weights for lower imbalance ratios. Crucially, despite the varying class distributions, the danger class recall consistently remained robust above 90.0% with acceptable precision. This confirms that the proposed framework is adaptable to different hazard characteristics rather than overfitted to a single specific distribution.

Table 5. Robustness validation under varying simulated imbalance ratios.

Simulated Imbalance Ratio	Adaptively Searched Optimal Weights (I:II:III:IV)	Danger Class Precision	Danger Class Recall
2324:1	1:2:10:60	0.967	0.922
1000:1	1:2:8:40	0.958	0.938
500:1	1:2:10:25	0.941	0.906
100:1	1:2:5:10	0.975	0.953

Feature importance ranking from the model (Figure 11) placed the newly constructed eccentric loading indices K_{STA} (0.209) and K_{AFC} (0.149) third and fourth, respectively, after mean borehole stress (0.315) and mean anchor cable load (0.229). Thus, the dimensionless asymmetry indices representing spatial load imbalance and stress transfer were more sensitive to roadway stability evolution, further corroborating the mechanism of asymmetric shear failure under eccentric loading.

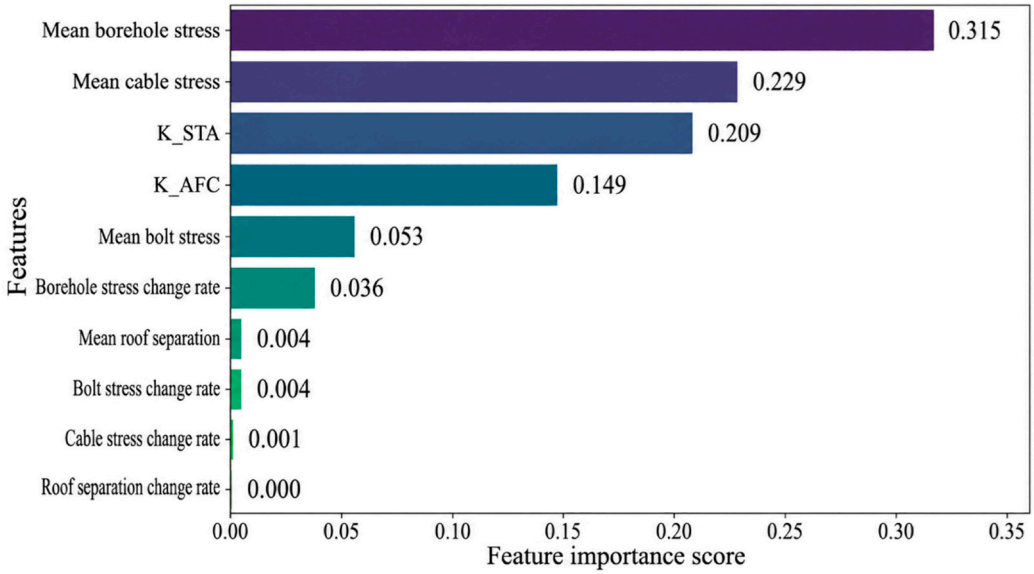

Figure 11. Mean borehole stress and new asymmetry indices dominate feature importance.

4.3. Roadway Safety Risk Zonation Based on Assessment Results

The pre-extraction ground-pressure time series from the 2206 return airway was input into the trained improved XGBoost model for retrospective safety assessment along the full roadway. Before differentiated reinforcement, the model identified 5435 Level III (warning) states and 114 Level IV (danger) states during the monitoring period (Figure 12). These hazards were strongly clustered in space. Station 12 (near 700 m), located in the zone affected by superimposed loading from the overlying coal pillar, was the most critical: it received 3660 Level III warnings and 50 Level IV danger events and was classified as an extremely high-risk eccentric loading zone. Station 01 (near 50 m), at the roadway entrance, received 884 Level III warnings and 42 Level IV danger events and was classified as a medium–high-risk zone. Station 07 (near 350 m), in the section affected by a goaf on one side, received 578 Level III warnings and no danger alarms and was classified as a medium-risk zone. Most other stations remained at Level I (safe) or Level II (attention) throughout the monitoring period.

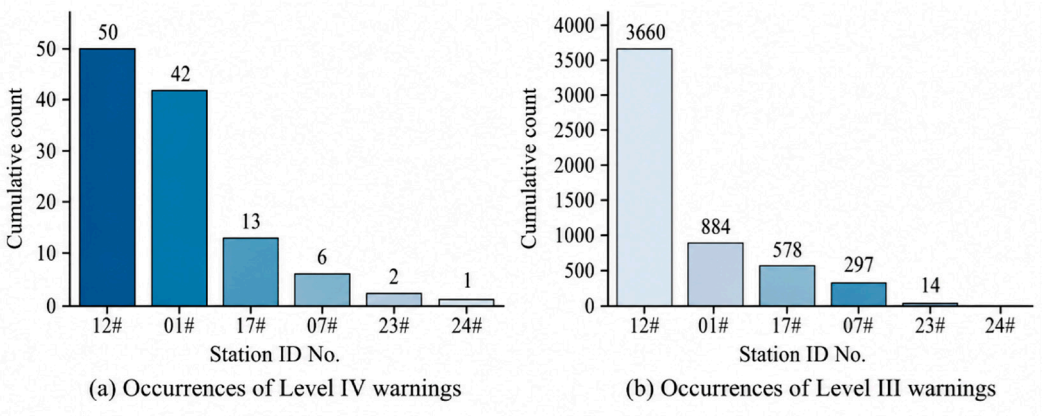

Figure 12. Level III and Level IV warnings were spatially concentrated at key monitoring stations.

Accordingly, the 2206 return airway was divided into four safety risk zones (Figure 13): high risk (chainage 650–750 m), medium–high risk (20–80 m), medium risk (320–380 m), and low risk (all remaining sections).

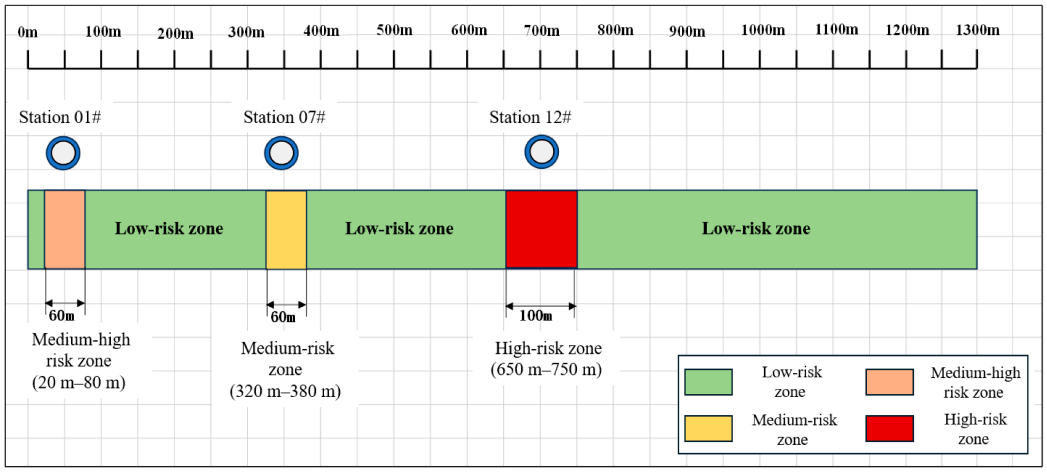

Figure 13. Improved XGBoost model delineates four roadway risk zones.

5. Differentiated Control of Roadway Surrounding Rock

5.1. Zone-Specific Differentiated Control Scheme

A zone-specific surrounding rock control strategy was developed to maintain stability of the 2206 return airway throughout its service life. Based on the numerical simulations and safety assessment, the 1300 m return airway was subdivided into three control zones (Figure 14a).

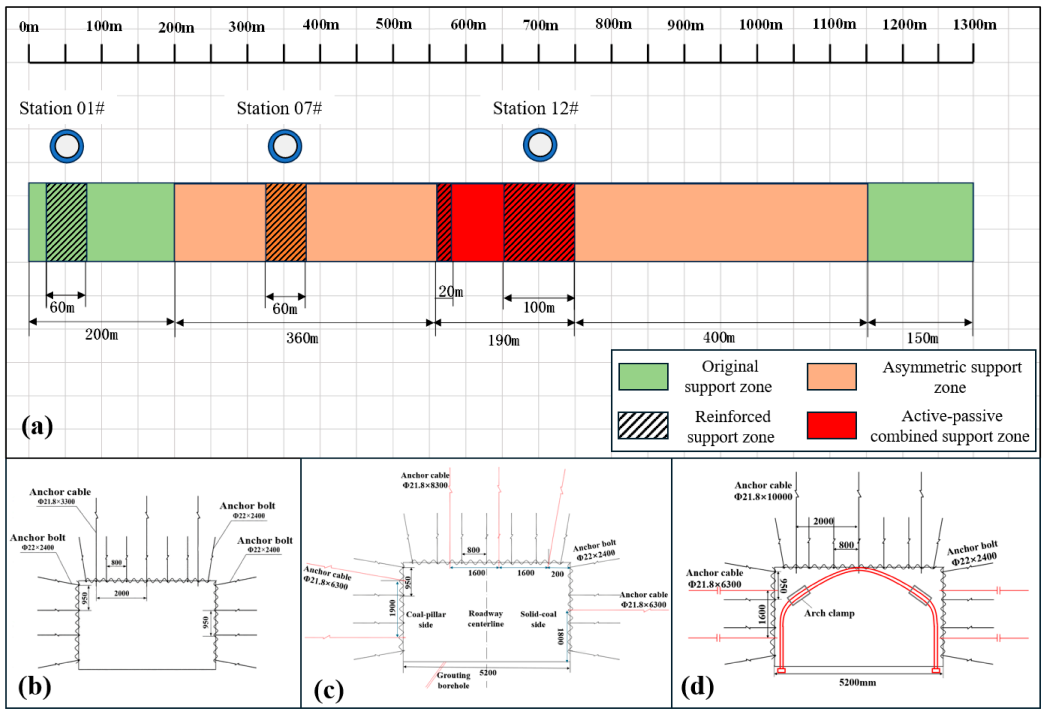

Figure 14. Three differentiated support zones target axial risk distribution. (**a**) Roadway zoning for differentiated support schemes; (**b**) Original roadway support scheme; (**c**) Asymmetric support scheme of the roadway; (**d**) Active-passive combined support scheme.

Level I conventional control zones (chainages 0–200 m and 1150–1300 m): Mining disturbance was limited in these zones, and the original symmetric anchor bolt–mesh–cable support was retained. The roof was supported symmetrically by Φ22 × 2400 mm threaded-steel anchor bolts at 800 × 900 mm spacing and Φ21.8 × 8300 mm flexible anchor cables

at 2000 × 1800 mm spacing. Both walls were supported symmetrically by threaded-steel anchor bolts of the same specification at 950 × 900 mm spacing (Figure 14b).

Level II asymmetric reinforcement zones (chainages 200–560 m and 750–1150 m): Lateral abutment pressure from the 2204 goaf produced asymmetric surrounding rock damage. Accordingly, asymmetric reinforcement was added to the conventional support system. Two Φ21.8 × 6300 mm high-capacity long anchor cables, inclined upward by 10°, were installed at the shoulder of the coal pillar side at a row spacing of 1900 mm. One long anchor cable of the same specification was installed at mid-height on the solid coal side, and floor grouting was applied to suppress asymmetric floor heave (Figure 14c).

Level III active–passive combined control zone (chainage 560–750 m): This zone was directly beneath the overlying 2301 goaf and was subjected to extreme superposition of static and dynamic eccentric loads. An active–passive support scheme comprising U36 yielding steel sets at 550 mm spacing and Φ21.8 × 10,000 mm high-capacity long anchor cables was therefore adopted (Figure 14d).

5.2. Field Monitoring Results

The effectiveness, rationality, and feasibility of the new support scheme were evaluated using data from the multi-source real-time monitoring network. Online monitoring data collected from 11 January to 10 February 2026, after implementation of the new support scheme, were input into the improved XGBoost roadway safety assessment model. The results are presented in Table 6.

Table 6. Roadway safety assessment results after reinforcement.

Risk Level	Occurrences
Danger	1
Warning	27
Attention	251

At Station 12 (near 700 m), previously classified as extremely high risk, the Level III active–passive combined support maintained both integrated asymmetry coefficient K_{AFC} and structural transfer asymmetry coefficient K_{STA} below the safety threshold of 0.2 throughout the monitoring period. No further Level IV danger alarm was triggered, indicating long-term stability of the surrounding rock in this severely eccentrically loaded section. At Stations 01 (near 50 m) and 07 (near 350 m), the Level II asymmetric reinforcement substantially reduced eccentric loading asymmetry. Station 01 triggered one Level IV danger warning during initial stress release after reinforcement but no subsequent Level IV danger or Level III warning alarm. At Station 07, the integrated asymmetry coefficient likewise remained below 0.2, and no instability was observed. The agreement between the field trial and model assessment indicates that the proposed zone-specific differentiated and asymmetric control method effectively mitigates butterfly-shaped rotational deformation of the island panel roadway beneath closely spaced seams and maintains structural safety during working-face extraction.

6. Conclusions

This study addressed the severe asymmetric deformation of an island panel roadway beneath a closely spaced coal seam under extreme eccentric loading from multiple goafs. By integrating physical mechanism analysis, spatial asymmetry feature extraction, cost-sensitive intelligent warning, and axial differentiated control, we developed a framework for long-term safety monitoring and stability control of roadways under complex eccentric loading.

(1) Differential subsidence of the bidirectional cantilever-hinged overburden structure, caused by nonuniform boundary support stiffness, was identified as the mechanical origin of the asymmetric roadway deformation. An eighth-order implicit equation for the plastic zone boundary was derived by jointly considering principal stress axis deflection angle and principal stress ratio. The analysis confirmed that the stress ratio controlled plastic zone development depth, whereas the deflection angle controlled its spatial rotational orientation, providing an analytical basis for interpreting heterogeneous failure along the roadway axis.

(2) Dimensionless physical indices centered on the integrated asymmetry coefficient and structural transfer asymmetry coefficient were constructed. These features transform difficult-to-measure parameters of deep principal stress axis deflection and loading imbalance into readily measurable load transfer indices for the near-surface surrounding rock support system. Pearson correlation and feature importance analyses showed that the two indices contributed independent information and were highly sensitive to imbalanced surrounding rock instability.

(3) A cost-sensitive XGBoost safety-state assessment model with nonlinear penalty weights was established to overcome classifier bias caused by the 2324:1 class imbalance in the time-series monitoring data. Forward rolling time-series cross-validation increased recall for danger samples from 37.5% for the baseline model to 92.2%, while precision reached 96.7%, substantially reducing missed detections of sudden low-probability hazards.

(4) A three-tier axial differentiated surrounding rock control method was developed by integrating stress evolution segments with intelligent risk zonation. The 1300 m return airway was divided into conventional support, asymmetric reinforcement, and active–passive combined control zones. Closed-loop verification using field tests and the intelligent assessment model showed that danger warnings along the full roadway fell to zero after differentiated support was implemented, while the integrated asymmetry coefficients at critically eccentrically loaded stations (e.g., Station 12 and Station 07) stabilized below 0.2 during the monitoring period. These results verified the effectiveness of the control scheme for severely deforming surrounding rock under eccentric loading.

Despite the promising results, this study focused on deterministic, single-target classification tailored to the specific eccentric loading conditions of the Xiaohuigou Coal Mine. First, the constructed physical surrogate features and the optimal cost-sensitive penalty weights remain highly dependent on local hazard characteristics, necessitating further validation using independent datasets from varied geological environments. Second, to better address sensor noise and geological variability, future work will aim to upgrade the current framework by exploring explicit uncertainty-aware assessments and advanced multi-target predictive architectures that integrate target variables into inputs.

Author Contributions: Conceptualization, W.F., Y.S. and X.F.; methodology, W.F. and Y.S.; software, D.H. and J.H.; validation, D.H. and J.H.; formal analysis, N.C.; investigation, N.C. and H.F.; data curation, J.F.; writing—original draft preparation, W.F. and Y.S.; writing—review and editing, Y.S. and D.H.; visualization, J.H. and H.F.; funding acquisition, X.F. All authors have read and agreed to the published version of the manuscript.

Funding: This work was supported in part by the National Natural Science Foundation of China under grant 52474183 and in part by the Fundamental Research Funds for the Central Universities under grant 2020ZDPY0209.

Institutional Review Board Statement: Not applicable.

Informed Consent Statement: Not applicable.

Data Availability Statement: The raw data supporting the conclusions of this article will be made available by the authors on request.

Acknowledgments: The authors gratefully acknowledge the Xiaohuigou Coal Mine for their support in conducting the field experiments. The authors also thank the editor and anonymous reviewers for their constructive suggestions and comments, which have considerably improved the quality of this paper.

Conflicts of Interest: The authors declare no conflicts of interest.

References

1. Li, S.; Lu, W.; Ma, X.; Mao, J.; Zheng, X.; Yang, C.; Feng, J. Study on deformation characteristics and support technology of roadway in deep complex stress field. *Sci. Rep.* **2026**, *16*, 7373. [CrossRef] [PubMed]
2. Huang, W.; Zhu, L.; Liu, Y.; Yuan, X.; Shen, J. Surrounding rock control of roadways under dynamic disturbances in closely spaced coal seams. *Geomech. Geophys. Geo-Energy Geo-Resour.* **2026**, *12*, 84. [CrossRef]
3. Carranza-Torres, C.; Fairhurst, C. Application of the convergence-confinement method of tunnel design to rock masses that satisfy the hoek-brown failure criterion. *Tunn. Undergr. Space Technol.* **2000**, *15*, 187–213. [CrossRef]
4. Vlachopoulos, N.; Diederichs, M.S. Improved longitudinal displacement profiles for convergence confinement analysis of deep tunnels. *Rock Mech. Rock Eng.* **2009**, *42*, 131–146. [CrossRef]
5. Diederichs, M.S. The 2003 canadian geotechnical colloquium: Mechanistic interpretation and practical application of damage and spalling prediction criteria for deep tunneling. *Can. Geotech. J.* **2007**, *44*, 1082–1116. [CrossRef]
6. Ma, Y.; Wang, W.; Yuan, C.; Liu, Q.; Tian, X.; Shu, S.; Ge, S. Research on mechanism and control technology of non-uniform evolution of plastic zone in roadway surrounding rock under dual mining disturbance: A case study. *Eng. Fail Anal.* **2026**, *196*, 111101. [CrossRef]
7. Fu, Q.; Yang, K.; He, X.; Liu, Q.; Wei, Z.; Wang, Y. Destabilization mechanism and stability control of the surrounding rock in stope mining roadways below remaining coal pillars: A case study in buertai coal mine. *Processes* **2022**, *10*, 2192. [CrossRef]
8. Huang, P.; Wu, B.; Topal, E.; Shao, H.; You, Z.; Ma, S.; Chen, R. Safety support design and sustainable guarantee method for gob-side roadway along thick coal seams. *Sustainability* **2025**, *18*, 346. [CrossRef]
9. Li, S.; Yin, Y.; Li, C.; Chen, B.; Huang, J.; Zhang, L. Stress distribution and energy-driven rock burst hazard assessment of coal pillars in gob-side entries. *Energy Explor. Exploit.* **2026**, *44*, 2537–2556. [CrossRef]
10. Zhu, Z.; Li, D. Stability assessment of long gateroad pillar in ultra-thick coal seam: An extensive field and numerical study. *Geomech. Geophys. Geo-Energy Geo-Resour.* **2022**, *8*, 147. [CrossRef]
11. Zhang, Q.; Wang, J.; Guo, Y.; Chen, Y.; Sun, Q. Study on deformation and stress evolution law of surrounding rock under repeated mining in close coal seam. *Energy Sources Part A—Recovery Util. Environ. Eff.* **2025**, *47*, 1550–1568. [CrossRef]
12. Ding, T.; Wang, W.; Zhang, C.; Zhang, W.; Chen, Y. Field investigation and stability analysis of gob-side roadway retention with an 8 m coal pillar in extra-thick coal seam mining. *Processes* **2026**, *14*, 2187. [CrossRef]
13. Huang, W.; Zhao, T.; Zhang, C.; Liu, Y.; Sui, L.; Hou, T.; Jang, D. Assessment of pillar stability and its control in a double roadway layout. *Energy Sci. Eng.* **2024**, *12*, 4192–4209. [CrossRef]
14. Sakhno, I.; Sakhno, S.; Skrzypkowski, K.; Isaienkov, O.; Zagorski, K.; Zagorska, A. Floor heave control in gob-side entry retaining by pillarless coal mining with anti-shear pile technology. *Appl. Sci.* **2024**, *14*, 4992. [CrossRef]
15. Kajzar, V.; Kukutsch, R.; Waclawik, P.; Nemcik, J. Innovative approach to monitoring coal pillar deformation and roof movement using 3D laser technology. In *ISRM European Rock Mechanics Symposium EUROCK 2017*; Konicek, P., Soucek, K., Konecny, P., Eds.; Elsevier Science Bv: Ostrava, Czech Republic, 2017; Volume 191, pp. 873–879. [CrossRef]
16. Singh, S.K.; Banerjee, B.P.; Raval, S. Three-dimensional unique-identifier-based automated georeferencing and coregistration of point clouds in underground mines. *Remote Sens.* **2021**, *13*, 3145. [CrossRef]
17. Lee, Y.-J. Investigation of subsurface deformations associated with model tunnels in a granular mass. *Tunn. Undergr. Space Technol.* **2009**, *24*, 654–664. [CrossRef]
18. Hudecek, V.; Sancer, J.; Zubicek, V.; Golasowski, J. Experience in the adoption of room & pillar mining method in the company OKD, a.s., czech republic. *J. Min. Sci.* **2017**, *53*, 99–108. [CrossRef]
19. Satici, O.; Topal, T. Assessment of damage zone thickness and wall convergence for tunnels excavated in strain-softening rock masses. *Tunn. Undergr. Space Technol.* **2021**, *108*, 103722. [CrossRef]
20. Zhu, Y.; Xue, H.; Liu, B.; Liu, Q.; Liu, X.; Liu, Q. Study on failure mechanical properties and acoustic emission characteristics of pre-damaged sandstone under cyclic loading. *Eng. Fail Anal.* **2026**, *195*, 111001. [CrossRef]
21. Zhan, K.; Wen, X.; Wang, X.; Kong, C. A method for characterization of stress concentration degree of coal mine roadway surrounding rock. *J. Geophys. Eng.* **2023**, *20*, 699–711. [CrossRef]

22. Wang, W.; Qiu, P.; Wang, K.; Zhang, X.; Jiang, Y.; Li, H. Occurrence mechanism and safety identification of the "muffled thunder" phenomenon in coal mine roadway. *Rock Mech. Rock Eng.* **2026**, *59*, 5387–5415. [CrossRef]
23. Fang, X.; He, D.; Wang, J.; Song, Y. Prediction of excavation damaged zone thickness in underground coal mine roadways using a PSO-stacking model. *Measurement* **2026**, *28*, 121929. [CrossRef]
24. Ibrahim, B.; Ahenkorah, I.; Ewusi, A. Explainable risk assessment of rockbolts' failure in underground coal mines based on categorical gradient boosting and SHapley additive exPlanations (SHAP). *Sustainability* **2022**, *14*, 11843. [CrossRef]
25. Li, G.; Ding, H.; Wang, K.; Zhang, X.; Sun, J. Intelligent recognition of muffled blasting sounds and lithology prediction in coal mines based on RDGNet. *Sensors* **2025**, *25*, 7601. [CrossRef] [PubMed]
26. Ma, T.; Zhang, Y.; Lei, D.; Wang, Y. Identification and classification prediction of microseismic signals from coal-rock fracture in deep coal mines. *Rock Mech. Rock Eng.* **2026**. [CrossRef]
27. Cui, F.; Zong, C.; Lai, X.; Jia, C.; Luo, Z. Prediction of coal burst location and risk level in roadway using XGBoost with multi-element microseismic information and its application in steeply inclined ultra-thick coal seam. *Rock Mech. Rock Eng.* **2025**, *58*, 4023–4042. [CrossRef]
28. Huang, D.; Li, W.; Chang, X.; Tan, Y. Key factors identification and risk assessment for the stability of deep surrounding rock in coal roadway. *Int. J. Environ. Res. Public Health* **2019**, *16*, 2802. [CrossRef] [PubMed]
29. Wang, S.; Yuan, C.; Li, L.; Su, X.; Wang, C. Application of Research on Risk Assessment of Roadway Roof Falls Based on Combined Weight Matter Element Extension Model. *Appl. Sci.* **2024**, *14*, 4111. [CrossRef]
30. Mikielewicz, M.; Kazemi, F.; Jankowski, R. Data-driven predictive model and uncertainty analysis of vehicle-induced vibrations based on experimental measurements. *Mech. Syst. Signal Process.* **2026**, *254*, 114336. [CrossRef]
31. Yin, S.; Han, K.; Wang, E.; Yan, Y.; Zhao, X. Research on optimal width of coal pillars in both sides of abandoned mining areas and tunnel control technology. *Energy Sci. Eng.* **2026**, *14*, 3625–3637. [CrossRef]
32. Xu, Y.; Pan, K.; Zhang, H. Investigation of key techniques on floor roadway support under the impacts of superimposed mining: Theoretical analysis and field study. *Environ. Earth Sci.* **2019**, *78*, 436. [CrossRef]
33. Khayrutdinov, M.M.; Ma, L.Q.; Mangi, H.N.; Kongar-Syuryun, C.; Klyuev, R.V.; Petenko, A.; Brigida, V. Ensuring decarbonization underground construction technologies of backfilling based on the tailings. *Constr. Mater. Prod.* **2026**, *9*, 7. [CrossRef]

Disclaimer/Publisher's Note: The statements, opinions and data contained in all publications are solely those of the individual author(s) and contributor(s) and not of MDPI and/or the editor(s). MDPI and/or the editor(s) disclaim responsibility for any injury to people or property resulting from any ideas, methods, instructions or products referred to in the content.